

A functional relation for field-scale nonaqueous phase liquid dissolution developed using a pore network model

Leslie A. Dillard^{a,*,1}, Hedef I. Essaid^b, Martin J. Blunt^{c,2}

^a Department of Geological and Environmental Sciences, Stanford University, Stanford, CA 94305-2115, USA

^b Water Resources Division, U.S. Geological Survey, 345 Middlefield Road, Menlo Park, CA 94025, USA

^c Department of Petroleum Engineering, Stanford University, Stanford, CA 94305-2220, USA

Received 15 April 1999; received in revised form 6 March 2000; received in revised form 31 July 2000;
accepted 5 September 2000

Abstract

A pore network model with cubic chambers and rectangular tubes was used to estimate the nonaqueous phase liquid (NAPL) dissolution rate coefficient, $K_{\text{diss}} a_i$, and NAPL/water total specific interfacial area, a_i . $K_{\text{diss}} a_i$ was computed as a function of modified Peclet number (Pe') for various NAPL saturations (S_N) and a_i during drainage and imbibition and during dissolution without displacement. The largest contributor to a_i was the interfacial area in the water-filled corners of chambers and tubes containing NAPL. When $K_{\text{diss}} a_i$ was divided by a_i , the resulting curves of dissolution coefficient, K_{diss} versus Pe' suggested that an approximate value of K_{diss} could be obtained as a weak function of hysteresis or S_N . Spatially and temporally variable maps of $K_{\text{diss}} a_i$ calculated using the network model were used in field-scale simulations of NAPL dissolution. These simulations were compared to simulations using a constant value of $K_{\text{diss}} a_i$ and the empirical correlation of Powers et al. [Water Resour. Res. 30(2) (1994b) 321]. Overall, a methodology was developed for incorporating pore-scale processes into field-scale prediction of NAPL dissolution. © 2001 Published by Elsevier Science B.V.

Keywords: NAPL; Mass transfer; Dissolved materials; Oil–water interface; Simulation

* Corresponding author. Systems Technology Associates, 14142 Denver West Pkwy, Suite 300, Golden, CO 80401, USA. Tel.: +1-303-271-1478 x208.

E-mail address: inogaret@staped.com (L.A. Dillard).

¹ Now Leslie A.D. Nogaret.

² Present address: The Center for Petroleum Studies, T.H. Huxley School for the Environment, Earth Science, and Engineering, Royal School of Mines, Imperial College of Science, Technology, and Medicine, Prince Consort Road, London SW72BP, England.

1. Introduction

Numerical modeling of field-scale dissolution of nonaqueous phase liquids (NAPLs) requires dissolution rate coefficients as input. NAPL dissolution rate coefficients are a function of properties such as aqueous flow rate and NAPL/water interfacial area (Borden and Kao, 1992; Geller and Hunt, 1993; Holman and Javandel, 1996; Hunt et al., 1988a,b; Imhoff et al., 1994; Johnson and Pankow, 1992; Kennedy and Lennox, 1997; Mackay et al., 1991; Mayer and Miller, 1992, 1993; Miller et al., 1990; Pfannkuch, 1984; Powers et al., 1991, 1992, 1994a,b; Priddle and MacQuarrie, 1994; Voudrias and Assaf, 1996; Voudrias and Yeh, 1994; Zaidel and Russo, 1993). Aqueous flow rate can be expressed as the dimensionless Peclet number (Pe), which represents a ratio of advective to diffusive effects:

$$Pe = \frac{q_w d_{50}}{D_m}, \quad (1)$$

where q_w = Darcy velocity [$L \ t^{-1}$], d_{50} = median grain size [L], and D_m = molecular diffusion coefficient of NAPL in water [$L^2 \ t^{-1}$].

The specific interfacial area, a_i , is defined as:

$$a_i = \frac{A_i}{V}, \quad (2)$$

where A_i = interfacial area [L^2], and V = porous medium volume [L^3].

Due to the difficulty involved in direct measurement, surrogate measures for NAPL/water interfacial area, such as NAPL saturation (S_N), have been proposed. However, Miller et al. (1990), Powers et al. (1992), and Schaefer et al. (2000b) have shown that interfacial area depends not only on S_N , but also on the direction of the saturation change (drainage or imbibition). Thus, a complex interdependency exists between the dissolution rate coefficient, Pe , S_N , and NAPL/water interfacial area. To simplify this complexity, much recent effort has been devoted to obtaining experimental values of NAPL/water or air/water interfacial area.

Gvirtzman and Roberts (1991) used an ideal soil model based on the concept of homogeneous arrangements of identical spheres for which a_i can be calculated when the wetting fluid is discontinuous. The method presented by Skopp (1985) was based on calculating the area of concave water interfaces. Karkare and Fort (1996) determined air/water a_i using a water-insoluble surfactant that spread as a monolayer at the interface. A film balance specified the interfacial area occupied by each surfactant molecule at a critical surfactant concentration. The air/water a_i was then calculated as the product of the number of surfactant molecules and the interfacial area occupied by each surfactant molecule at the critical surfactant concentration. Saripalli et al. (1997a,b, 1998) and Kim et al. (1997) developed an interfacial tracer method to estimate NAPL/water and air/water a_i in two-phase systems using a water-soluble anionic surfactant. The mass of surfactant sorbed at the interface was determined by measuring the retardation factor of surfactant that was advectively transported through the column.

The Gibbs adsorption equation (Rosen, 1989), along with measurements of air/water or NAPL/water interfacial tension, were used to obtain a_i . Recently, Schaefer and Blunt (2000) and Schaefer et al. (2000a,b) developed a method to measure air/water or NAPL/water a_i during gravity drainage and secondary imbibition or at residual NAPL saturation, S_{rN} , in two- and three-phase systems. A column was divided into horizontal slices. Within each slice, the mass of water and surfactant was obtained using a gas chromatograph and UV detector, respectively. These data were used in the Gibbs adsorption equation and in a surfactant mass balance equation to obtain a_i over a range of water saturations.

Other methods have focused on the relation between a_i , and the capillary pressure–water saturation function (P_c-S_w), where P_c [$M L^{-1} t^{-2}$] is defined through the Young–Laplace equation as:

$$P_c = \frac{2\sigma_{Nw}\cos\theta}{r_{Nw}}, \quad (3)$$

where σ_{Nw} = NAPL/water interfacial tension [$M t^{-2}$], r_{Nw} = NAPL/water radius of curvature [L], and θ = contact angle (zero for a strongly water-wet system).

Lowry and Miller (1995) used a pore network model to investigate a_i at residual water saturation, S_w . Cary (1994) used the P_c-S_w relation to estimate a pore size distribution considering porous media as a bundle of capillary tubes. The total a_i was then obtained by summing the interfacial area for each drained capillary tube at that P_c . Alternatively, Bradford and Leij (1997), Hassanizadeh and Gray (1990, 1993), Leverett (1941), and Miller et al. (1990) used a thermodynamic approach that estimated a_i from measured P_c-S_w curves.

The P_c-S_w functional relation is generally different for drainage and imbibition displacements (Dullien, 1992). Hassanizadeh and Gray (1990) alternatively proposed that a formal relationship exists between capillary pressure, water saturation, and total specific interfacial area, or a $P_c-S_w-a_i$ surface. Hassanizadeh and Gray (1993) hypothesized that the hysteretic P_c-S_w function was an artifact of projecting the $P_c-S_w-a_i$ surface onto the P_c-S_w plane.

Reeves and Celia (1996) systematically investigated this hypothesis in a network modeling study. They found that indeed the $P_c-S_w-a_i$ functional relation is consistently smooth and well behaved, which implies that direct estimates of NAPL/water interfacial area could be predicted given information regarding the capillary pressure and saturation of the system under study. Furthermore, they believed that the smoothness of their simulation results suggested that the $P_c-S_w-a_i$ relation may be fundamental to multiphase systems and provided a verification of the hypothesis of Hassanizadeh and Gray (1990). However, Reeves and Celia (1996) also found that the $P_c-S_w-a_i$ relation is nonunique; for example, for any value of capillary pressure, there exist two points with different water saturation and the same interfacial area.

There are two advantages of using a pore network model instead of other methods to estimate a_i : first, all pertinent processes, such as flow, transport, and nonequilibrium dissolution, can be represented simultaneously in the network model using simple physical laws; and second, the network model can be used to investigate the full range

of saturations that may be difficult to obtain experimentally. However, network models have limitations as well. A limitation of the Reeves and Celia (1996) study was that their network model used spherical pore bodies and conical pore throats. They could not represent pendular fluid that would be found in a natural pore network with pores and pore throats of angular cross-section, with grain-to-grain contact. Reeves and Celia (1996) suggested that future work should focus on the impact of pendular wetting fluid on interfacial area and saturation.

In this work, we use a pore network model with pores and pore throats of square cross-section to explore the complex relationship between the NAPL dissolution rate coefficient, Pe , S_N , and a_i . Cubic pore bodies and throats of square cross-section allow for the evaluation of pendular liquids as found in natural porous media. We hypothesize that the dissolution rate coefficient is dependent on Pe , S_N , and a_i , resulting in a dissolution relation similar in complexity to the $P_c-S_w-a_i$ surface of Reeves and Celia (1996). We use a pore network model that was developed to study NAPL dissolution (Dillard and Blunt, 2000) and validated using NAPL dissolution data (Powers, 1992). The network model is used to generate dissolution relations for a range of S_N , a_i , and Pe . A value of the dissolution rate coefficient obtained from the dissolution relation for particular conditions of S_N , a_i , and Pe is used as input for a grid block having these same conditions in a field-scale simulator. Lastly, the utility of the dissolution relation developed using the pore network model is shown in a hypothetical modeling exercise of field-scale NAPL dissolution. This paper is organized into the following sections: Section 2 contains a brief description of the network model; Section 3 contains dissolution relation results; Section 4 contains application of the dissolution relation in a field-scale model; and Section 5 contains conclusions.

2. Pore network model

2.1. Development and validation

The pore network model used in this study was developed to study NAPL dissolution (Dillard and Blunt, 2000). The network model idealizes a porous medium as a three-dimensional lattice of cubic chambers (pores) that are connected to other chambers by tubes (pore throats) with square cross-sections. The square cross-sections, which provide a conduit for water flow around NAPL blobs, serve as surrogates for the roughness and grooves in a real porous medium. We assume in our NAPL/water simulations that the solid in the network model is water-wet. We also assume a constant coordination number of six; that is, six tubes surround every chamber.

The network model is able to simulate drainage and imbibition, two-phase flow, and solute transport. To ensure the network pore size distribution was representative of a real porous medium, the probability distribution functions that determine tube radii and lengths were adjusted such that the simulated styrene–water P_c-S_w curves generated by the network model matched the experimental curves of Powers (1992). In this work, the inscribed radius of a cubic chamber or square tube is referred to as the chamber or tube radius. Chamber radii were assigned to be equal to the greater of either the largest

neighboring tube radius, or the product of the average neighboring tube radius and aspect ratio. The aspect ratio, a_r , is defined as the ratio of chamber to tube radii, and is assumed to be 1.7. No other matching parameters were used in the network model. The drainage and imbibition P_c – S_w curves were generated using a network initially saturated with water. The network NAPL/water radius of curvature (r_{Nw}) for each displacement step was equivalent to the inscribed radius of the chamber or tube displaced in that step. The network capillary pressure was then obtained through the Young–Laplace equation (Eq. (3)). The experimental curves reflected a residual water saturation in the experimental column. Residual water saturation was generated in the network model using a trapping rule that identified a chamber as trapped if it was surrounded by NAPL-filled tubes. Trapped fluid had a pressure equivalent to the network capillary pressure when the region became trapped.

Two-phase flow was represented in the network by adapting Poiseuille's Law for flow in a pipe. Solute transport was represented by applying the equation for solute mass flux, F [$M\ t^{-1}$], to the network tubes and solving for concentrations, C [$M\ L^{-3}$], in the chambers:

$$F = Q_w C - D_m A_w \frac{\partial C}{\partial x}, \quad (4)$$

where Q_w = aqueous phase volumetric flow rate [$L^3\ t^{-1}$], and A_w = water cross-sectional area in tube [L^2].

We assumed complete mixing of solute in the chambers (Dillard and Blunt, 2000). The transfer of the dissolved NAPL components across the NAPL/water interface into the water corner is conceptualized as a one-dimensional diffusion process called corner diffusion (Zhou et al., 2000). Consider the NAPL-filled chamber in Fig. 1a, where the dissolved NAPL concentration exiting the NAPL-filled chamber C_i^{out} , is a function of the NAPL concentration entering the chamber C_i^{in} , and a term representing the transfer of NAPL concentration across the NAPL/water interface:

$$C_i^{out} = C_i^{in} + E_d (C_s - C_i^{in}), \quad (5)$$

where C_s is the NAPL solubility. Fig. 1b shows a cross-section of the NAPL-filled chamber in Fig. 1a. Fig. 1b also shows a water corner of this chamber, and a one-dimensional representation of this water corner. In Fig. 1b, water flows perpendicular into the page. E_d is defined as the normalized average dissolved NAPL concentration in the corner and is a function of a dimensionless time, t_d , that represents the duration of contact between an NAPL blob and the water flowing in the corner:

$$E_d = \sqrt{t_d} \left[\text{ierfc} \left(\frac{-\sqrt{t_d}}{2} \right) - \text{ierfc} \left(\frac{1-t_d}{2\sqrt{t_d}} \right) \right], \quad (6)$$

where

$$t_d = \frac{l_b}{\xi^2} \frac{D_m}{v_{wc}}, \quad (7)$$

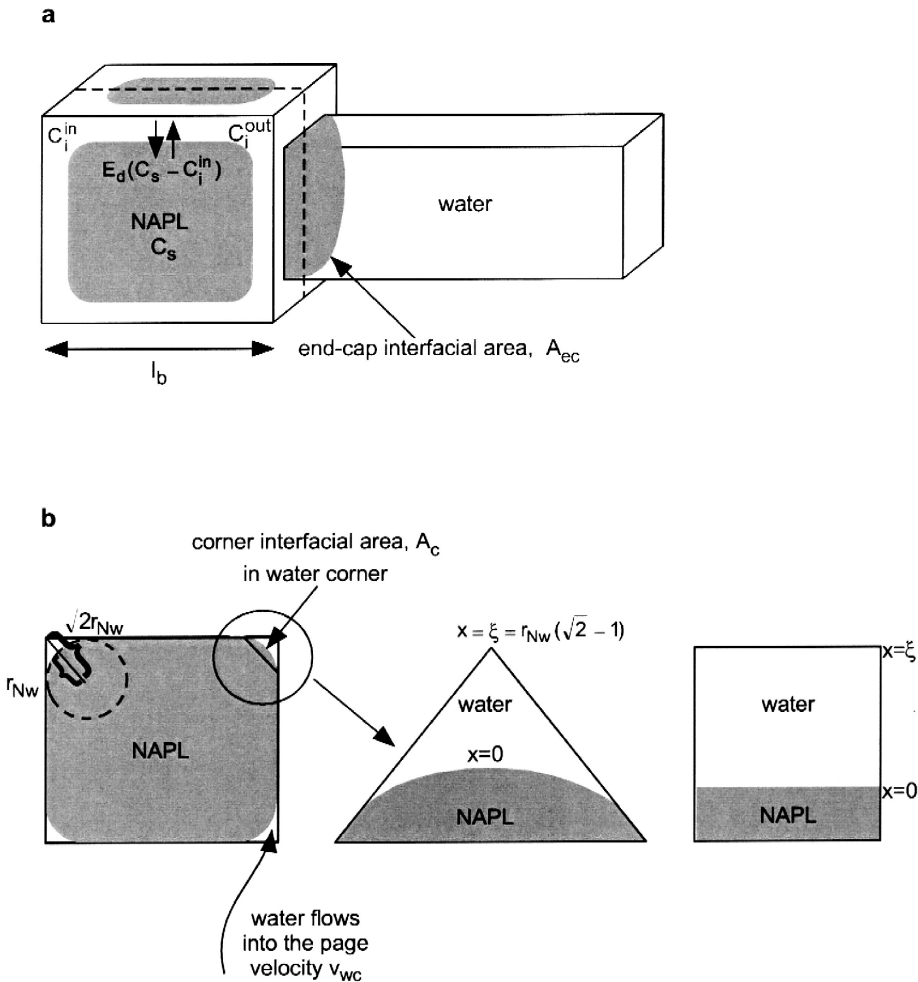


Fig. 1. Schematics of (a) an NAPL-filled chamber and a water-filled tube depicting end-cap interfacial area, and (b) a cross-section of the NAPL-filled chamber showing corner interfacial area with enlargement of the water corner and a one-dimensional representation of the water corner. The cross-section in (b) corresponds to the dotted line in (a).

and l_b = blob length [L], ξ = corner length [L], v_{wc} = velocity of water in corners [L t^{-1}], and $\text{ierfc}(x) = \int_x^\infty \text{erfc}(\xi) d\xi$ is the integral complementary error function and is tabulated in Carslaw and Jaeger (1959).

All of the parameters in the expression for t_d (Eq. (7)) can be calculated in every NAPL-filled chamber or tube based on pore and fluid geometries. Fig. 1a and b show representations of l_b , ξ , and v_{wc} . Fig. 2 shows the normalized average dissolved NAPL corner concentration, E_d , versus dimensionless time, t_d . Corner diffusion is the dominant process in NAPL dissolution at the high flow rates characteristic of NAPL

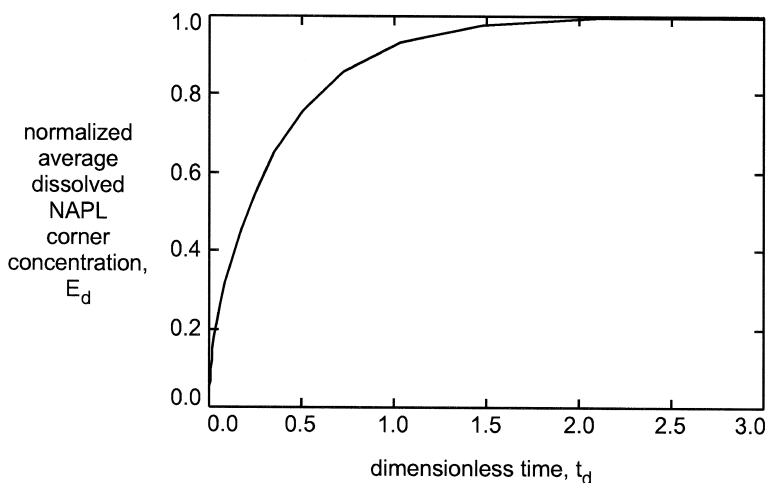


Fig. 2. Normalized average dissolved NAPL corner concentration, E_d , versus dimensionless time, t_d .

dissolution experiments (Zhou et al., 2000). More details regarding the derivation of E_d and t_d , and the concept of corner diffusion, can be found in Zhou et al. (2000).

Data from a dissolution experiment with residual styrene blobs established in a uniform, coarse-grained Wagner #18 sand (Powers, 1992) were used to validate the network model. The normalized NAPL effluent concentration data, C/C_s , were used to obtain the dissolution rate coefficient, $K_{\text{diss}} a_i$, using:

$$K_{\text{diss}} a_i = -\frac{q_w}{L} \ln \left(1 - \frac{C}{C_s} \right), \quad (8)$$

where C = NAPL effluent concentration [M L^{-1}], C_s = styrene solubility ($T = 20\text{--}23^\circ\text{C}$) (Powers et al., 1992), L = column length [L], and K_{diss} = NAPL dissolution coefficient [L t^{-1}].

In previous studies such as Imhoff et al. (1994), Miller et al. (1990), and Powers et al. (1991, 1992, 1994a,b), $K_{\text{diss}} a_i$ is referred to as the mass transfer rate coefficient; in this work, we refer to it as the dissolution rate coefficient. Fig. 3 shows network model simulated and experimental curves for $K_{\text{diss}} a_i$ versus Pe . Unless otherwise stated, the results presented here are for a 20-cubed network model ($NX = 20$, $NY = 20$, $NZ = 20$ chambers). More details of the development and validation of NAPL dissolution in the network model can be found in Dillard and Blunt (2000).

2.2. Interfacial area

Previous work using a pore network model (Lowry and Miller, 1995; Reeves and Celia, 1996) suggested that a complex relation exists between capillary pressure and interfacial area. In these studies, the network tubes and chambers had circular cross-sections that did not allow for water-filled corners. NAPL/water interfacial area was

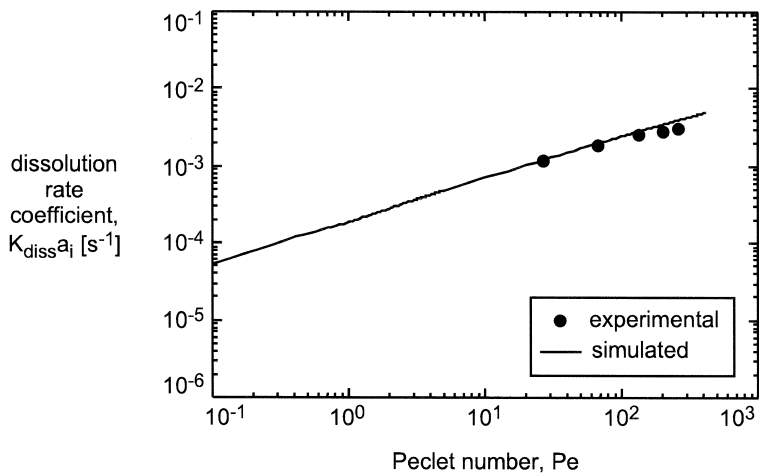


Fig. 3. Experimental and simulated NAPL dissolution rate coefficient versus Peclet number.

represented as the end cap between a tube and chamber where one contains NAPL and the other contains water. Fig. 1a shows a schematic of end-cap interfacial area, A_{ec} , between an NAPL-filled chamber and a water filled-tube. We assign the end-cap interfacial area to the tube, A_{ec}^t , or chamber, A_{ec}^c , containing NAPL (Lowry and Miller, 1995):

$$A_{ec}^c = A_{ec}^t = 2\pi r_c \left(r_c - \sqrt{r_c^2 - r_t^2} \right), \quad (9)$$

where r_c = chamber radius; r_t = tube radius.

The A_{ec}^c and A_{ec}^t for all chambers and tubes containing NAPL are then summed and the total, A_{ec} , is divided by the network volume, V , to obtain the end-cap specific interfacial area, a_{ec} :

$$a_{ec} = \frac{A_{ec}}{V}. \quad (10)$$

The shape parameters of the probability distribution functions for tube radii and lengths presented in Dillard and Blunt (2000) were used to obtain the results shown in Fig. 3. However, because we are interested in studying interfacial area over the full range of saturations, the trapping rule of Dillard and Blunt (2000) for residual water saturation was not used in this study. The values of residual styrene saturation with trapping of water and without were $S_{rN} = 0.2058$ and 0.2286 , respectively.

Fig. 4 shows the network NAPL/water a_{ec} versus S_N for drainage and imbibition. The endpoints of the drainage curve represent single-phase systems, and thus the a_{ec} values are zero. The overall shape of the drainage curve in Fig. 4 looks similar to the primary drainage curve of air/water a_{ec} versus water saturation, S_w , published by Reeves and Celia (1996). The absolute magnitude of a_{ec} , however, is greater for the Reeves and Celia (1996) study than for this work. In particular, the maximum values of

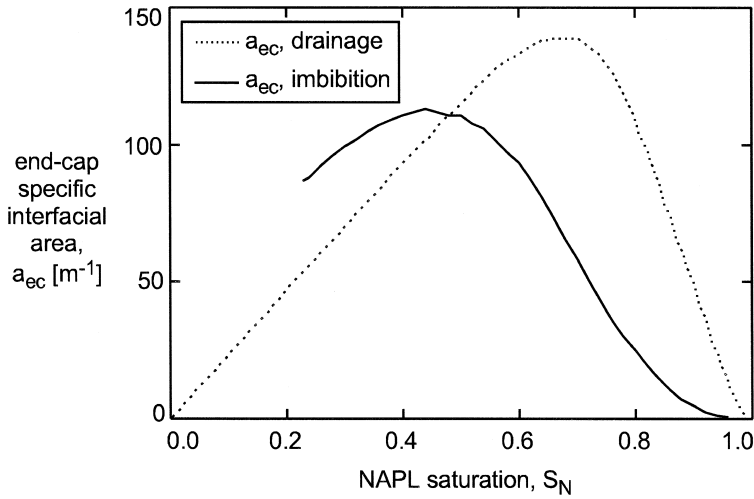


Fig. 4. Network model end-cap specific interfacial area versus NAPL saturation for drainage and imbibition.

end-cap interfacial area for primary drainage are $a_{ec} = 267 \text{ m}^{-1}$ at $S_w = 0.271$ and $a_{ec} = 139 \text{ m}^{-1}$ at $S_w = 0.298$ for Reeves and Celia (1996) and this work, respectively. The discrepancy is most likely due to different pore sizes as reflected by the magnitude of capillary pressure for Reeves and Celia (1996) ($P_c \approx 5000 \text{ Pa}$ at $S_w = 0.271$) and this work ($P_c \approx 343 \text{ Pa}$ at $S_w = 0.298$). In addition, the different pore geometry (spherical chambers and biconical tubes) and different representation of imbibition used in Reeves and Celia (1996) could contribute to the discrepancy in the maximum value of a_{ec} . However, in view of the considerable uncertainty in pore size, pore geometry, and imbibition mechanism, the maximum values of a_{ec} reported by Reeves and Celia (1996) and for this study are quite similar.

We introduce another interfacial area formed by the NAPL/water interface in the corners of chambers and tubes that contain both NAPL and water phases. Fig. 1b shows a schematic of this corner interfacial area, A_c . Corner interfacial areas for a chamber, A_c^c , and a tube, A_c^t , are defined as:

$$A_c^c = 2\pi r_{Nw} l_c, \quad (11)$$

$$A_c^t = 2\pi r_{Nw} l_t, \quad (12)$$

where chamber length, l_c , and tube length, l_t , are defined assuming the NAPL in a chamber or tube is cylindrical in shape:

$$l_c = \frac{V_N^c}{(2r_c)^2 - ((2r_{Nw})^2 - \pi r_{Nw}^2)}, \quad (13)$$

$$l_t = \frac{V_N^t}{(2r_t)^2 - ((2r_{Nw})^2 - \pi r_{Nw}^2)}. \quad (14)$$

V_N^c and V_N^t represent the NAPL volume in a chamber and tube, respectively. The A_c^c and A_c^t for all chambers and tubes containing NAPL are then summed and the total, A_c , is divided by the network volume, V , to obtain the corner specific interfacial area, a_c :

$$a_c = \frac{A_c}{V}. \quad (15)$$

The end-cap and corner specific interfacial areas are summed to obtain the total specific interfacial area, a_i :

$$a_i = a_{ec} + a_c. \quad (16)$$

Fig. 5 shows curves of NAPL/water a_i , a_c , and a_{ec} versus S_N for drainage and imbibition. The curves of a_{ec} versus S_N are the same as in Fig. 4. Fig. 5 shows that the magnitudes of the imbibition curves are significantly higher than for the drainage curves for both a_i and a_c . This is because for a given saturation, the capillary pressure is much lower in imbibition than in drainage, corresponding to a higher value of r_{Nw} (Eq. (11)).

The overall shape of the a_i and a_c curves, with minima at $S_N = 0.0$ and 1.0 and a maximum at an intermediate S_N value, can be explained using Fig. 6a and b. The corner specific interfacial area is a function of the NAPL/water radius of curvature, r_{Nw} (Eqs. (11) and (12)). At high P_c and S_N , NAPL is squeezed into the corners of the pore space (Fig. 6a), leading to small r_{Nw} and a_c . Conversely, at low P_c and S_N , the large NAPL/water interfacial area in the corners (Fig. 6b) is offset by the small number of blobs, resulting in a small a_c . At intermediate P_c and S_N , a_c appears to hit a maximum. a_i exhibits similar behavior because it is dominated by a_c .

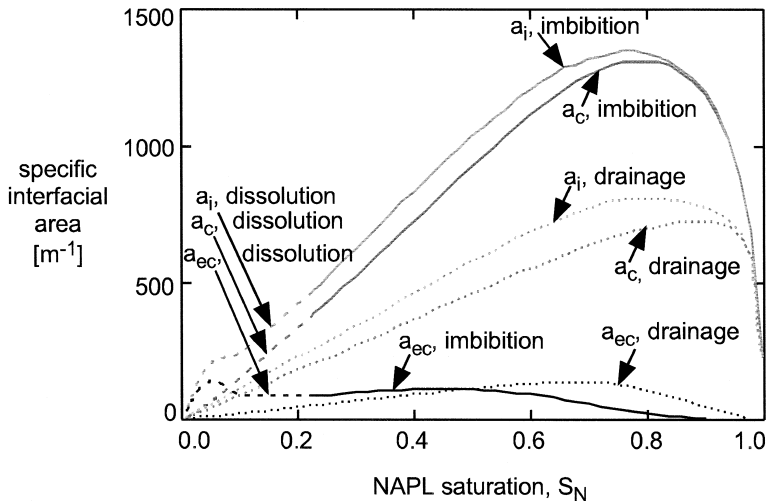


Fig. 5. Network model end-cap (a_{ec}), corner (a_c), and total (a_i) specific interfacial area versus NAPL saturation for drainage (dotted line), imbibition (solid line), and dissolution without displacement (dashed line).

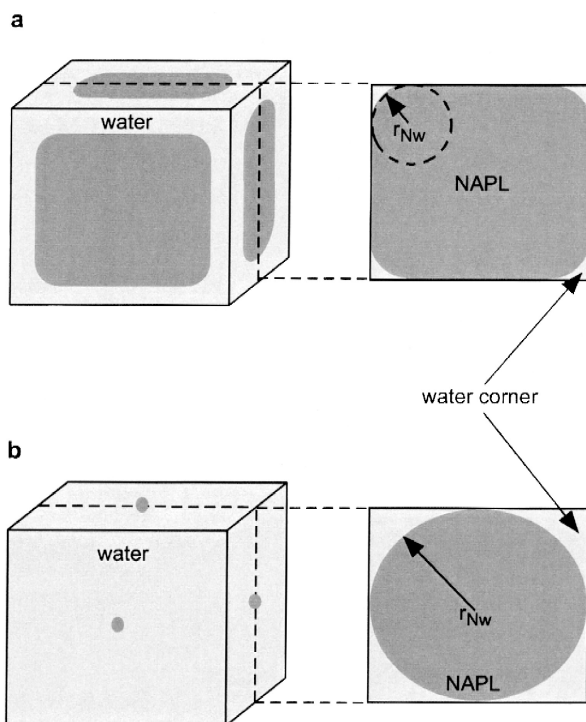


Fig. 6. Schematics of NAPL and water in a network model chamber at (a) high capillary pressure, and (b) low capillary pressure.

Recently, Schaefer and Blunt (2000) obtained indirect measurements of NAPL/water interfacial area at residual NAPL saturation. They compared their measured value of $a_i = 1.17 \text{ m}^{-1}$ obtained at $S_{rN} = 0.18$ to a_i obtained using our network model scaled to reflect the porous medium used in their experiments. They calculated the scaled network $a_i = 1.85 \text{ m}^{-1}$ at $S_{rN} = 0.2286$. Considering the network model was not designed to match the experiments, it is encouraging that the theoretical and experimental values of a_i are of the same magnitude.

For completeness, the curves in Fig. 5 for a_i , a_c and a_{ec} for imbibition are continued from $S_{rN} = 0.2286$ to 0. These curves were obtained by dissolving the residual NAPL blobs and are labeled as dissolution curves. This dissolving NAPL simulation was conducted by flushing the network model with water at a constant Darcy velocity of $4.39 \times 10^{-5} \text{ m/s}$. The concentration field was computed. For a time step corresponding to a pore volume, the amount of mass removed from an NAPL-filled chamber or tube was calculated from the dissolution flux in the chamber or tube. The amount of mass removed from an NAPL-filled chamber or tube was used to recalculate the new decreased NAPL mass. This new NAPL mass was used to find the new NAPL volume. We assumed that the NAPL dissolved in length in both the chambers and tubes. A new length of NAPL in a chamber or tube was calculated after each time step by assuming

the NAPL/water radius of curvature was constant and using Eqs. (13) and (14). These new lengths were used in Eqs. (11) and (12) to compute corner interfacial area for chambers and tubes, respectively. End-cap interfacial area was computed using Eq. (9), and the end-cap and corner interfacial areas were summed to obtain the total interfacial area.

Note that the a_c dissolution curve decreases to zero from the residual NAPL saturation obtained at the end of the imbibition displacement. However, the a_{ec} dissolution curve has a peak at $S_N = 0.05$ indicating an increase in end-cap specific interfacial area (Fig. 4). This increase in a_{ec} corresponds to the exposure of an end cap in an NAPL-filled tube following total dissolution of NAPL in a neighboring network chamber.

The most striking feature of Fig. 5 is that a_c is much larger than a_{ec} , except at very low S_N . This suggests that the corner specific interfacial area, and not end-cap specific interfacial area, is the key contributor to the total specific interfacial area. Previous work has shown (Dillard and Blunt, 2000) and others have suggested (Reeves and Celia, 1996) that corner geometry in network tubes and chambers is crucial for realistic representation of fundamental physics. Fig. 5 shows the importance of corner geometry in the calculation of total specific interfacial area.

3. Dissolution relation results

3.1. Effect of NAPL saturation and hysteresis

Experimental $K_{diss} a_i$ data are often obtained at residual NAPL saturation (Guarnaccia et al., 1992; Imhoff et al., 1994; Miller et al., 1990; Parker et al., 1991; Pfannkuch, 1984; Powers et al., 1991, 1992, 1994a,b). However, higher saturations, or lower saturations due to partial dissolution, may be encountered in the field. A predictive expression is therefore needed to obtain dissolution rate coefficients for all NAPL saturations.

The definition of Peclet number in Eq. (1) as a function of Darcy velocity was appropriate for application to a column experiment (Fig. 3). In our field-scale simulations, however, it was simpler to find $K_{diss} a_i$ as a function of a modified Peclet number, Pe' , that is a function of the average linear velocity, v_w :

$$Pe' = \frac{v_w d_{50}}{D_m}, \quad (17)$$

where $v_w = (q_w / \phi S_w)$.

The network model was used to generate a physically based relation between dissolution rate coefficient and Pe' for high and low NAPL saturations, hereafter referred to as the dissolution relation. The dissolution relation for high NAPL saturations ($S_N \geq S_{rN}$) was obtained during drainage and imbibition at $S_N = 0.4$ and 0.6 , and at $S_{rN} = 0.2286$ following imbibition. The dissolution relation for low NAPL saturations

($S_N < S_{rN}$) was obtained at $S_N = 0.1, 0.08, 0.06, 0.04$, and 0.02 . Note that the low NAPL saturations in these curves were obtained by dissolving the residual NAPL in the network model down to the appropriate value of S_N using the method described in Section 2.2.

Fig. 7a shows $K_{diss} a_i$ versus Pe' obtained at $S_N \geq S_{rN}$. The $K_{diss} a_i$ values for the $S_{rN} = 0.2286$ curve are the same as for the curve in Fig. 3; however, note that Fig. 3 displays Pe and Fig. 7a displays Pe' . Fig. 7b shows $K_{diss} a_i$ versus Pe' obtained at $S_N < S_{rN}$. The constant NAPL volume experimental data shown in Fig. 3 would correspond to Pe' of 75, 187, 373, 560, and 739 in Fig. 7a and b. Because nonequilibrium conditions were achieved in the experiment at these Pe' , these Pe' represent the range of interest in NAPL dissolution. Furthermore, $K_{diss} a_i$ is poorly defined for $Pe' < 1$ and for high S_N because $C \rightarrow C_s$ everywhere under these conditions (Eq. (8)). However, Fig. 7a and b are extended to low Pe' for completeness. Together, Fig. 7a and b depict a representation of the dissolution relation at the NAPL saturations shown.

Fig. 7a and b could be used to obtain a value of $K_{diss} a_i$ for input in a field-scale simulator. However, the significant spread in the suite of curves requires that information regarding S_N , Pe' , and hysteresis, be obtained. The suite of dissolution relations is indeed complex. In an effort to simplify this complexity, we obtained the dissolution coefficient itself, K_{diss} , by dividing $K_{diss} a_i$ by the total specific interfacial area, a_i .

Fig. 8a shows K_{diss} versus Pe' obtained at $S_N \geq S_{rN}$. Fig. 8b shows K_{diss} versus Pe' obtained at $S_N < S_{rN}$. In the range of Pe' corresponding to the experimental data, a_i generally increases with each curve of increasing S_N in Fig. 8a and b. In comparison to Fig. 7a and b, the spread of the K_{diss} versus Pe' curves in Fig. 8a and b, most notably at high Pe' , was significantly reduced, indicating that the dissolution coefficient is weakly a function of NAPL saturation or hysteresis. The weak dependence of K_{diss} on S_N and hysteresis indicates dissolution behavior is a function of the NAPL distribution obtained following wetting and drying histories. However, because K_{diss} is mostly dependent on Pe' , an approximate value of K_{diss} could be obtained from Fig. 8a or b independent of S_N and hysteresis. Then, if a measurement of total specific interfacial area for the porous medium can be obtained using methods reported recently in the literature (Karkare and Fort, 1996; Kim et al., 1997; Saripalli et al., 1997a,b, 1998; Schaefer and Blunt, 2000, Schaefer et al., 2000a,b), the product ($K_{diss} a_i$) would yield a value of the dissolution rate coefficient for input in a field-scale simulator. However, although measurements of a_i are now possible, they are not easily obtainable. Thus, the dissolution relation in Fig. 7a and b should be used, along with S_N , Pe' , and hysteresis information, to obtain $K_{diss} a_i$.

Recall that the network model used to obtain the dissolution relation presented in Fig. 7a and b was developed with tube and chamber size distributions such that the network simulated capillary pressure curves matched the experimental curves obtained by Powers (1992) for a uniform coarse-grained sand. Indeed, the flat slope of the experimental and simulated P_c-S_w curves in Dillard and Blunt (2000) reflected the homogeneity of the uniform sand. The tube and chamber size distributions for a more heterogeneous porous medium would likely result in a different dissolution relation than Fig. 7a and b. In particular, the dependence of the dissolution relation for a heterogeneous porous medium on S_N and hysteresis may be more pronounced, resulting in a suite of curves of $K_{diss} a_i$

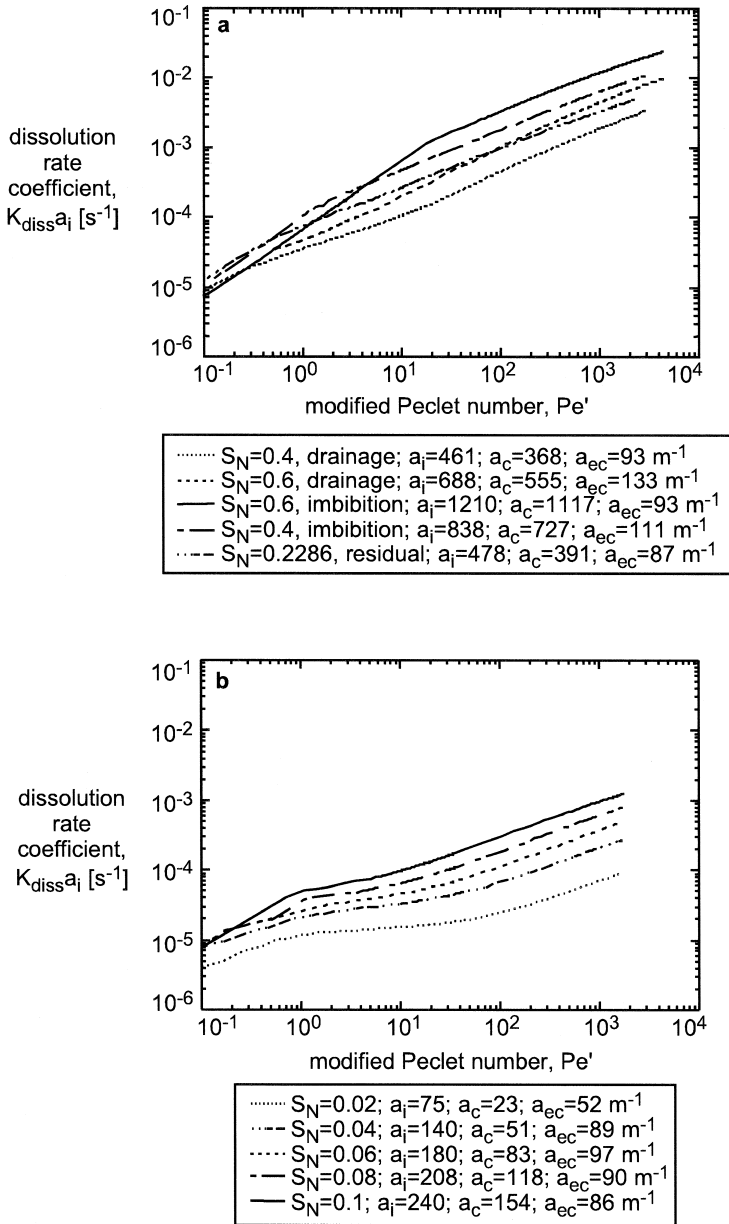


Fig. 7. The dissolution relation — a suite of curves of dissolution rate coefficient versus modified Peclet number for (a) high NAPL saturations, $S_N \geq S_{rN}$, and (b) low NAPL saturations, $S_N < S_{rN}$.

versus Pe' that have more spread than those in Fig. 7a. However, because a_i would also reflect the heterogeneous porous medium through its dependence on the tube and

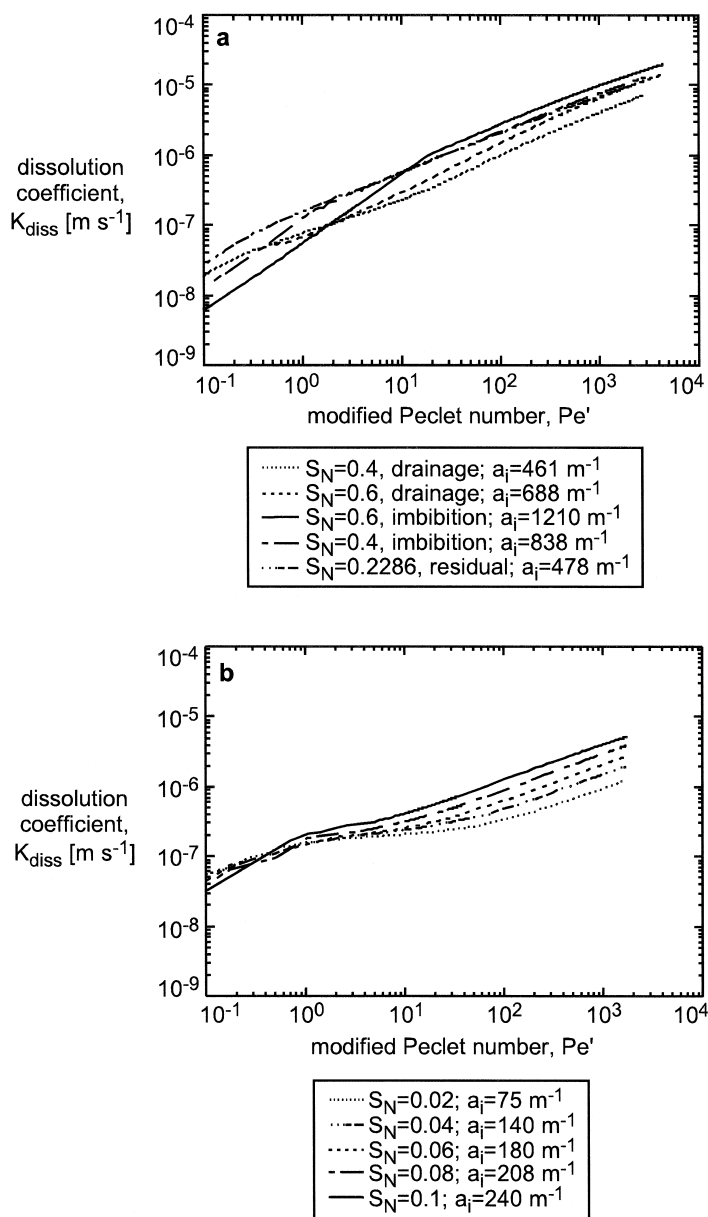


Fig. 8. Suite of curves of dissolution coefficient versus modified Peclet number for (a) high NAPL saturations, $S_N \geq S_{rN}$, and (b) low NAPL saturations, $S_N < S_{rN}$.

chamber size distributions, the curves of K_{diss} versus Pe' would likely be a weak function of S_N and hysteresis, similar to Fig. 8a and b. More simulations using a

network model based on a heterogeneous porous medium would be necessary to confirm these hypotheses.

In addition to K_{diss} , two other dissolution coefficients were obtained by dividing the dissolution rate coefficient by a representation of specific interfacial area: the end-cap dissolution coefficient, $K_{\text{diss}}^{\text{ec}}$, was obtained by using a_{ec} ; and the corner dissolution coefficient, $K_{\text{diss}}^{\text{c}}$, was obtained by using a_{c} . The similarity between the K_{diss} versus Pe' curves in Fig. 8a and b and the $K_{\text{diss}}^{\text{c}}$ versus Pe' curves indicated that a_{c} is the main contributor to a_i . By dividing the dissolution rate coefficient by a_{c} to obtain $K_{\text{diss}}^{\text{c}}$, we in essence normalized the curves by removing the effect of a_{c} . Dillard and Blunt (2000) showed that corner diffusion is the dominant mechanism controlling NAPL dissolution at high Pe' . In the high- Pe' regime characteristic of most NAPL dissolution experiments, corner diffusion, and its counterpart, a_{c} , are the key influences on NAPL dissolution.

3.2. Comparison with the Powers correlation

A conventional approach to estimating $K_{\text{diss}}a_i$ is to use an empirically based correlation expression developed using NAPL dissolution experimental data. Powers et al. (1994b) published a correlation expression to estimate $K_{\text{diss}}a_i$ for a Wagner #18 sand:

$$K_{\text{diss}}a_i = \frac{D_{\text{m}}}{d_{50}^2} \alpha Re'^{\beta_1} \delta^{\beta_2} U_i^{\beta_3} \left(\frac{\theta_{\text{N}}}{\theta_{\text{iN}}} \right)^{\beta_4} \quad (18)$$

where: $Re' = (v_{\text{w}} \rho_{\text{w}} d_{50}) / \mu_{\text{w}} =$ modified Reynold's number [–], $v_{\text{w}} =$ average linear velocity [L t^{-1}], $\rho_{\text{w}} =$ water density [M L^{-3}], $\mu_{\text{w}} =$ water viscosity [$\text{M L}^{-1} \text{t}^{-1}$], $U_i = d_{60}/d_{10}$ uniformity index [–], d_i ($i = 10, 50, 60$) = i th% of particles smaller than size d_i , $\delta = d_{50}/d_{\text{M}} =$ normalized grain size [–], $d_{\text{M}} =$ diameter of a “medium” sand grain (Powers et al., 1994b), $\theta_{\text{N}} =$ NAPL volumetric content [–], and $\theta_{\text{iN}} =$ initial NAPL volumetric content [–].

Table 1 shows relevant fluid and porous medium properties for Eq. (18). Values of the coefficients α , β_1 , β_2 , β_3 , β_4 and their 95% confidence intervals were determined

Table 1

Properties of fluids and Wagner #18 sand used in the Powers^a correlation

	Definition	Value
ρ_{w}	Water density [kg/m^3]	1000.0
μ_{w}	Water viscosity [$\text{kg m}^{-1} \text{s}^{-1}$]	0.00089
C_{s}	TCE solubility [kg/m^3] ($T = 20\text{--}23^\circ\text{C}$)	1.27
D_{m}	Molecular diffusion of TCE in water [m^2/s]	8.8×10^{-10}
d_{50}	Median grain size [m]	1.2×10^{-3}
d_{M}	Diameter of “medium” sand grain [m]	5.0×10^{-4}
U_i	Uniformity index [–]	1.19
θ_{iN}	Initial volumetric NAPL content	0.05

^aPowers et al. (1994b).

by a stepwise multiple regression technique (Powers, 1992) for the Wagner #18 sand: $\alpha = 4.13 (\pm 1.01)$; $\beta_1 = 0.598 (\pm 0.073)$; $\beta_2 = 0.673 (\pm 0.156)$; $\beta_3 = 0.369 (\pm 0.119)$; $\beta_4 = 0.902 (\pm 0.004)$.

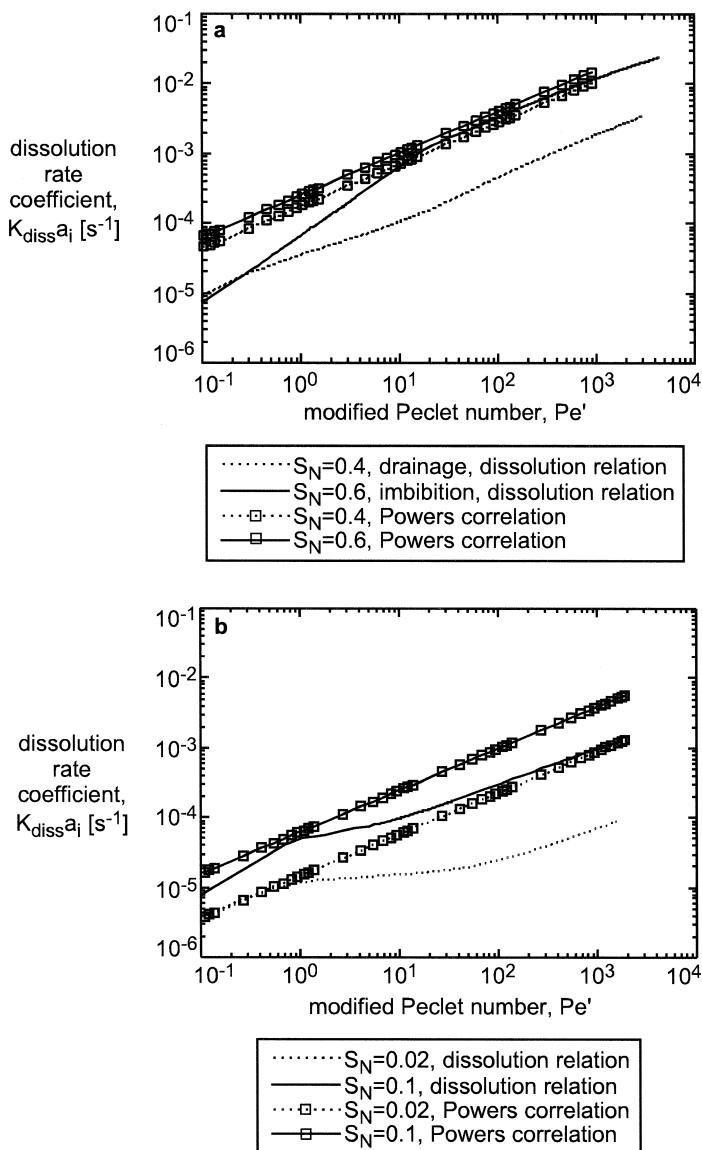


Fig. 9. Dissolution rate coefficient versus modified Peclet number obtained using the physically based dissolution relation (Fig. 7) and the empirically based Powers correlation (Eq. (18)) for (a) high NAPL saturations, $S_N \geq S_{rN}$, and (b) low NAPL saturations, $S_N < S_{rN}$.

Fig. 9a shows a comparison of the $S_N \geq S_{rN}$ dissolution relation and the Powers correlation for $S_N = 0.4$ (drainage) and 0.6 (imbibition). Fig. 9b shows a comparison of the $S_N < S_{rN}$ dissolution relation and the Powers correlation for $S_N = 0.1$ and 0.02. The dissolution relation curves are the same as in Fig. 7a and b for $S_N \geq S_{rN}$ and $S_N < S_{rN}$, respectively. For simplicity, only the bounding curves are shown with the highest and lowest $K_{diss} a_i$ in the Pe' range of data collection (75–739). The dissolution relation and the Powers correlation at S_{rN} were identical in the $Pe' = 75–739$ range.

Although it is uncertain whether the dissolution relation or Powers correlation is a better method to estimate $K_{diss} a_i$ outside of the range of data collection, some general observations can be made. Fig. 9a shows that the Powers correlation and the dissolution relation obtained during imbibition are quite similar. However, the dissolution relation obtained during drainage is approximately an order of magnitude smaller than the Powers correlation. Furthermore, the Powers correlation is in general an order of magnitude greater than the dissolution relation for $S_N < S_{rN}$ (Fig. 9b). The dissolution relation is presented as an alternative to the Powers correlation with some possible advantages. The dissolution relation curves account for hysteresis. And, whereas the Powers correlation was developed at S_{rN} and extended to $S_N \geq S_{rN}$, each curve of the dissolution relation was obtained at and is applicable at that S_N .

Note that whereas the Powers curves are straight, the curvature of the dissolution relation curves reflects the influence of different physical mechanisms on dissolution. Most notably, the curvature in the dissolution relation at the high Pe' characteristic of nonequilibrium dissolution experiments ($Pe' = 75–739$) is due to corner diffusion (Zhou et al., 2000).

As hypothesized, the relationship between $K_{diss} a_i$, S_N , Pe' , and a_i is very complex. But this complex dissolution relation can be simplified to two key ideas: NAPL dissolution is controlled by corner diffusion and a_c , and approximate values of K_{diss} can be obtained as a weak function of S_N or hysteresis. In the absence of an interfacial area measurement, the dissolution rate coefficient, $K_{diss} a_i$, can be obtained from the dissolution relation in Fig. 7a and b as a function of S_N and Pe' . This value of $K_{diss} a_i$ may then be used in a field-scale simulator to calculate local dissolution in a model grid block with the corresponding values of S_N and Pe' .

4. Application of the dissolution relation in a field-scale model

4.1. Model overview

In modeling field-scale NAPL dissolution, it may not be adequate to use a constant value of $K_{diss} a_i$, but instead it may be necessary to vary $K_{diss} a_i$ as S_N and Pe' change. Publications of hypothetical field-scale modeling of NAPL dissolution exist (e.g. Anderson et al., 1992; Borden and Pivoni, 1992; Brusseau 1992; Mayer and Miller, 1996; Priddle and MacQuarrie, 1994; Seagren et al., 1992; Sleep and Sykes, 1989) and other models incorporating nonequilibrium dissolution have been proposed (e.g. Delshad et al., 1996). A limitation of these studies is that either $K_{diss} a_i$ is independent of S_N and

Pe' , or $K_{\text{diss}}a_i$ varies with S_N and Pe' according to an empirically based correlation expression. Such correlation expressions are developed based on specific experimental data and may not be transferable to S_N and Pe' outside of the range studied experimentally, as shown in Section 3.2.

Our physically based dissolution relation is an alternative to empirically based correlation expressions. We used the dissolution relation in Fig. 7b to obtain values of $K_{\text{diss}}a_i$ for input in a field-scale model. For each model grid block containing NAPL, a value of $K_{\text{diss}}a_i$ was obtained via interpolation from the dissolution relation using the values of Pe' and S_N in the grid block. The curve for a particular S_N was used until the next smaller S_N was reached in a model grid block. This technique resulted in a spatially variable map of $K_{\text{diss}}a_i$ that also changed temporally as residual NAPL dissolved. This alternative approach to estimating $K_{\text{diss}}a_i$ values for input in a simulator is very easy to implement; any field-scale simulator that models nonequilibrium NAPL dissolution using an empirically based correlation expression such as that of Powers et al. (1994b) to obtain values of $K_{\text{diss}}a_i$ can be modified to use instead the physically based dissolution relation.

As noted in Section 3.1, the network model predictions of $K_{\text{diss}}a_i$ are sensitive to the distribution of chamber and tube sizes. In this section, we assume that the model parameters that gave a good match to the dissolution experiments of Powers (1992) can be used in this hypothetical field study. In general, however, the network model should use a pore size distribution representative of the porous media present at the field site of interest. The method of developing a network model that is representative of a porous medium is described in Dillard and Blunt (2000).

The spatially variable map of $K_{\text{diss}}a_i$ was used in a field-scale model modified to simulate nonequilibrium NAPL dissolution. The field-scale simulator used in this study was BIOMOC (Essaid et al., 1995; Essaid and Bekins, 1997). BIOMOC is a version of an existing two-dimensional flow and particle-tracking transport code (MOC) originally developed by Konikow and Bredehoeft (1978) and Goode and Konikow (1989) that was modified to include a representation of biodegradation by Monod kinetics (Monod, 1949). In this study, the Monod reaction terms were used not to represent biodegradation, but to represent NAPL dissolution from an immobile NAPL source. Appendix A contains a brief description of how BIOMOC was modified to represent NAPL dissolution.

4.2. Model application

BIOMOC was applied to a simple areal map of unit depth of a hypothetical site contaminated by trichloroethylene (TCE) that had been partially remediated, with discontinuous fractions of TCE left behind. The dimensions of the system in the longitudinal and transverse directions are 10-m long and 3-m wide, respectively; discretization is 0.05 m in both directions. A realization of hydraulic conductivity (K_{cond}) (Fig. 10) consisting of $K_{\text{cond}} = 1.0 \times 10^{-2}$ m/s with interbedded lenses of $K_{\text{cond}} = 3.0 \times 10^{-3}$ m/s was generated using an indicator-based simulation (SISIMPDF) from the GSLIB software package (Deutsch and Journel, 1992). The realization contains

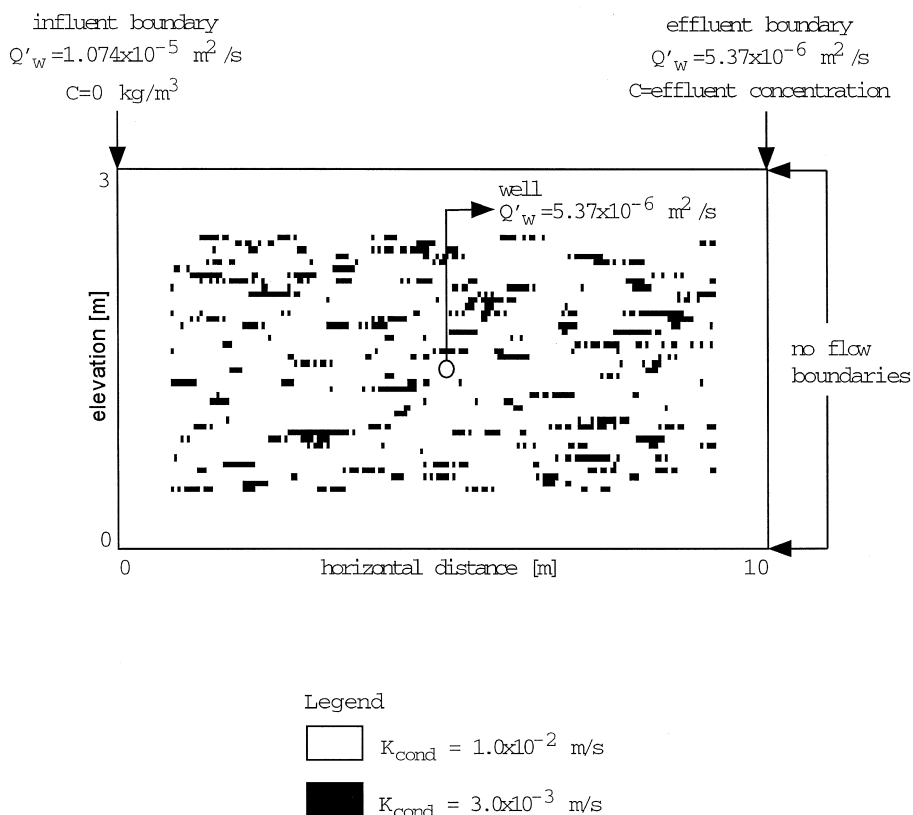


Fig. 10. Realization of hydraulic conductivity for the areal map of a hypothetical TCE-contaminated site. Boundary conditions for solution of the flow and transport equations are also shown.

10% lenses that have longitudinal and transverse correlation lengths of 0.5 and 0.05 m, respectively. Because the higher-permeability pathways were swept during remediation, we assumed that the TCE was contained in the low-permeability lenses at residual $S_N = 0.1$. To enhance stability in the particle tracking simulations, a border of $K_{\text{cond}} = 1.0 \times 10^{-2} \text{ m/s}$ was added around the areal map to avoid discontinuities in hydraulic conductivity at the boundaries.

Boundary conditions for solution of the flow equation in BIOMOC were specified flow boundaries at the left and right of the areal map (longitudinal direction), and no-flow boundaries on the top and bottom of the map (transverse direction). The flow per unit depth in each inlet grid block was $Q'_w = 1.85 \times 10^{-7} \text{ m}^2/\text{s}$, corresponding to the average linear velocity of 1 m/day characteristic of the Cape Cod field site (Hess et al., 1992). The total flow per unit depth at the influent boundary was $Q'_w = 1.074 \times 10^{-5} \text{ m}^2/\text{s}$. A line sink, hereafter referred to as a well, was placed in a water-saturated grid block in the center of the map (5.0, 1.5 m) and extracted fluid at the rate of $Q'_w = 5.37 \times 10^{-6} \text{ m}^2/\text{s}$. The resulting flow per unit depth at the effluent boundary was

$Q'_w = 5.37 \times 10^{-6} \text{ m}^2/\text{s}$. Boundary conditions for solution of the transport equation were $C = 0 \text{ kg/m}^3$ at the influent boundary, and the concentration of the water exiting the map was equal to the concentration at the location of the sink. Boundary conditions are labeled in Fig. 10. The initial condition for solution of the transport equation of dissolved TCE was $C = 0 \text{ kg/m}^3$ everywhere. The effective porosity of the areal map was 0.32. The mass balance error of all simulations was no more than 5%.

We designed three simulation cases to explore the utility of the dissolution relation: a simulation using a map of constant $K_{\text{diss}} a_i = 4.33 \times 10^{-4} \text{ s}^{-1}$; a simulation using a variable map of $K_{\text{diss}} a_i$ determined from the dissolution relation in Fig. 7b; and a simulation using a variable map of $K_{\text{diss}} a_i$ determined from the Powers correlation in Eq. (18). The map of constant $K_{\text{diss}} a_i$ was calculated using the $S_N = 0.1$ curve in Fig. 7b and a Pe' corresponding to $Q'_w = 1.85 \times 10^{-7} \text{ m}^2/\text{s}$. Model parameters for all three cases are summarized in Table 2.

Fig. 11 shows the normalized TCE effluent concentration versus time for the three simulation cases. Fig. 11 suggests that using a constant value of $K_{\text{diss}} a_i$, or a variable value of $K_{\text{diss}} a_i$ obtained from either the dissolution relation or the Powers correlation yields similar results. The maximum contaminant level (MCL) for TCE is $5 \text{ } \mu\text{g/l}$ or $5 \times 10^{-6} \text{ kg/m}^3$ (Montgomery, 1996), corresponding to a normalized MCL of 3.9×10^{-6} . In Fig. 11, the normalized TCE concentration leaving the effluent boundary reaches the MCL at similar times for all three cases: 162, 172, and 174 days for the constant $K_{\text{diss}} a_i$, dissolution relation, and Powers correlation cases, respectively. These clean-up times are shorter than the times reported in the literature for various types and distributions of NAPLs and flow conditions (Holman and Javandel, 1996; Mayer and

Table 2
Model parameters for hypothetical field-scale simulations

	Definition	Value
NX	Number of longitudinal cells	200
NY	Number of transverse cells	60
Δx	Longitudinal discretization [m]	0.05
Δy	Transverse discretization [m]	0.05
K_{cond}	Hydraulic conductivity [m/s]	Fig. 10
ε	Effective porosity	0.32
α_L	Longitudinal dispersivity [m]	0.15
α_T	Transverse dispersivity [m]	0.015
anis	Anisotropy	1.0
Δt	Time step [days]	0.365
ρ_N	TCE density [kg/m^3]	1.47×10^3
C_s	TCE solubility [kg/m^3] ($T = 20\text{--}23^\circ\text{C}$)	1.27
D_m	Molecular diffusion of TCE in water [m^2/s]	8.8×10^{-10}
d_{50}	Median grain size [m]	1.2×10^{-3}
S_N	NAPL saturation	0.1
$K_{\text{diss}} a_i$	Dissolution rate coefficient [s^{-1}]	4.33×10^{-4a} , Fig. 7b ^b , Eq. (18) ^c

^aConstant $K_{\text{diss}} a_i$.

^bDissolution relation.

^cPowers correlation (Powers et al., 1994b).

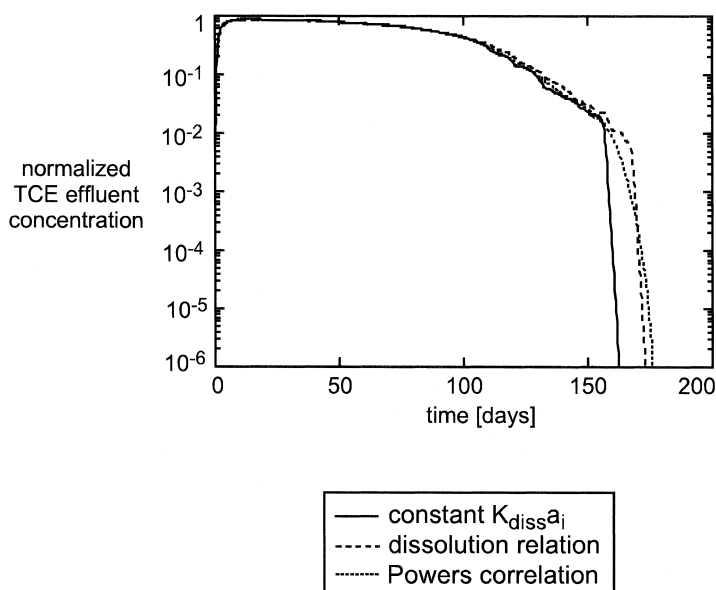


Fig. 11. BIOMOC simulation results of normalized TCE concentration versus time at the effluent boundary for cases of constant dissolution rate coefficient (constant $K_{\text{diss}} a_i$), and temporally and spatially variable dissolution rate coefficients obtained using the dissolution relation (Fig. 7b) and the Powers correlation (Eq. (18)). Flow boundary conditions at the inlet and effluent boundaries are $Q'_w = 1.074 \times 10^{-5} \text{ m}^2 \text{ s}^{-1}$ and $Q'_w = 5.37 \times 10^{-6} \text{ m}^2 \text{ s}^{-1}$, respectively, with $Q'_w = 5.37 \times 10^{-6} \text{ m}^2 \text{ s}^{-1}$ at the well.

Miller, 1996; VanderKwaak and Sudicky, 1996; Voudrias and Yeh, 1994; Whelan et al., 1994). The shorter clean-up times shown in Fig. 11 are most likely due to higher flow rate, lower NAPL mass, and because dissolution occurs from NAPL lenses rather than from an NAPL pool.

The similarity of the curves and clean-up times in Fig. 11 is likely due to equilibrium concentrations existing nearly throughout the areal map at all times. Only near the well are aqueous phase flow velocities high enough for nonequilibrium conditions to occur. The Pe' in grid blocks at the influent boundary, effluent boundary, and well are approximately 16, 8, and 500, respectively. Fig. 9b shows that at low- Pe' grid blocks, the dissolution relation and Powers correlation yield similar values of $K_{\text{diss}} a_i$. However, at high- Pe' grid blocks, the dissolution relation and Powers correlation yield $K_{\text{diss}} a_i$ values that differ by an order of magnitude. Likewise, the difference between the constant $K_{\text{diss}} a_i$ value that was obtained from the $S_N = 0.1$ curve in Fig. 7b and the $K_{\text{diss}} a_i$ values obtained using the Powers correlation becomes significant only at high- Pe' . Thus, the constant $K_{\text{diss}} a_i$, dissolution relation, and Powers correlation cases yield different grid-block values of $K_{\text{diss}} a_i$ and thus normalized TCE effluent concentration at the high- Pe' grid blocks near the well. However, these near-well nonequilibrium effects are averaged at the effluent boundary, resulting in normalized TCE effluent concentration versus time curves in Fig. 11 that are very similar for all three cases.

Consider, instead, an example with no extraction well and flow boundary conditions of $Q'_w = 1.074 \times 10^{-3} \text{ m}^2/\text{s}$ at the influent and effluent boundaries, corresponding to a groundwater velocity of 100 m/day and a Pe' between 1576 and 1752, depending on the value of S_w (Eq. (17)). The very high Pe' indicates that the system is stressed to a possibly unrealistic limit. However, this example is intended to illustrate the case with high aqueous phase flow velocities and thus, nonequilibrium conditions throughout the entire areal map. This example was simulated using the hydraulic conductivity map in Fig. 10 for the constant $K_{\text{diss}} a_i$, dissolution relation, and Powers correlation cases. Fig. 12 shows the normalized TCE effluent concentration versus time for the three simulation cases.

In Fig. 12, the shorter clean-up time for the Powers correlation compared to the dissolution relation is due to the higher $K_{\text{diss}} a_i$ predicted by the Powers correlation (Fig. 9b). The shorter clean-up time of the constant $K_{\text{diss}} a_i$ case compared to the dissolution relation or the Powers correlation cases can also be explained by Fig. 9b. Recall that the value of $K_{\text{diss}} a_i$ for the constant $K_{\text{diss}} a_i$ case was obtained at $S_N = 0.1$ from the dissolution relation curve in Fig. 9b. This value is likely to be too high at low S_N . Thus, the over-prediction of $K_{\text{diss}} a_i$ for the constant $K_{\text{diss}} a_i$ case, particularly at low S_N , results in a shorter clean-up time than for the dissolution relation or the Powers correlation cases.

Mayer and Miller (1996) conducted a detailed sensitivity analysis using different empirical correlation expressions to obtain $K_{\text{diss}} a_i$ for input into a field-scale simulator.

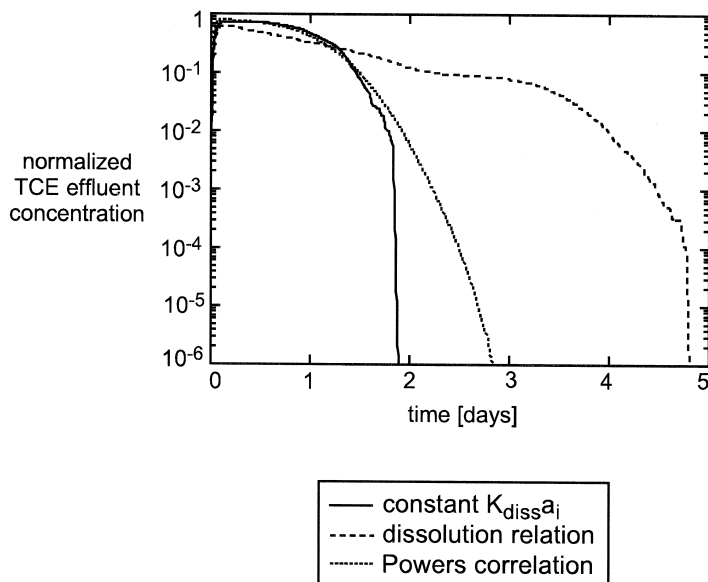


Fig. 12. BIOMOC simulation results of normalized TCE effluent concentration versus time for cases of constant dissolution rate coefficient (constant $K_{\text{diss}} a_i$), and temporally and spatially variable dissolution rate coefficients obtained using the dissolution relation (Fig. 7b) and the Powers correlation (Eq. (18)). Flow boundary conditions per unit depth at the influent and effluent boundaries are $Q'_w = 1.074 \times 10^{-3} \text{ m}^2/\text{s}^{-1}$.

Their simulation results of NAPL mass remaining versus dimensionless time were very similar for all empirical correlations, except for a correlation obtained from an experimental column containing heterogeneous media, and for simulations using a spatially variable hydraulic conductivity realization. This present work suggests that field-scale simulation of NAPL dissolution is insensitive to the method used to find $K_{\text{diss}} a_i$, except for simulations with high aqueous phase velocities and nonequilibrium dissolution everywhere. However, we have not performed a detailed sensitivity analysis, but have merely illustrated the utility of the physically based dissolution relation as an alternative to other methods to obtain $K_{\text{diss}} a_i$ for input into a field-scale simulator. A more detailed analysis with realistic field-scale examples is needed to ascertain the appropriateness of the physically based dissolution relation versus other methods to obtain $K_{\text{diss}} a_i$.

5. Conclusions

This work presents a physically based dissolution relation to predict NAPL dissolution rate coefficient ($K_{\text{diss}} a_i$) as a function of NAPL saturation (S_N), NAPL/water total specific interfacial area (a_i), and aqueous phase velocity in the form of a modified Peclet number (Pe'). A pore network model with cubic chambers and rectangular tubes that was developed to study NAPL dissolution (Dillard and Blunt, 2000) was used to investigate the influence of interfacial area on $K_{\text{diss}} a_i$. The total interfacial area was represented as the sum of an end-cap interfacial area across tube/chamber junctions and a corner interfacial area in the water corners of an NAPL-filled tube or chamber. While previous work has focused only on the end-cap interfacial area, we showed that corner interfacial area was the key contributor to total interfacial area. Thus, a network model with chambers and tubes of angular cross-section is crucial for a realistic representation of interfacial area.

When $K_{\text{diss}} a_i$ was divided by the total specific interfacial area, a_i , the resulting curves of dissolution coefficient, K_{diss} , versus Pe' suggested that an approximate value of K_{diss} could be obtained as a weak function of hysteresis or S_N . The product of K_{diss} and a measurement of a_i would yield an estimate of $K_{\text{diss}} a_i$ for input in a field-scale simulator. However, in the absence of an interfacial area measurement, $K_{\text{diss}} a_i$ can be obtained from the dissolution relation as a function of S_N and Pe' .

The dissolution relation of $K_{\text{diss}} a_i$ versus Pe' for various values of S_N developed at the network-model scale was used to obtain spatially and temporally variable maps of $K_{\text{diss}} a_i$ for input in field-scale simulations of NAPL dissolution. Field-scale simulation results using maps of constant and variable $K_{\text{diss}} a_i$ were compared. The variable $K_{\text{diss}} a_i$ cases were obtained using either the dissolution relation or the empirical correlation of Powers et al. (1994b). In general, simulation results of dissolved NAPL concentration versus time were similar for the dissolution relation and the Powers correlation. However, compared to the dissolution relation, the Powers correlation estimated a higher dissolution rate at high Pe' . A more detailed analysis with realistic field-scale examples is needed to ascertain the appropriateness of the physically based dissolution relation versus other methods to obtain $K_{\text{diss}} a_i$.

Overall, a methodology was developed for incorporating the pore-scale process of corner diffusion into field-scale prediction of NAPL dissolution via a pore network model. This methodology is a flexible tool that can be used to gain insight into a variety of other phenomena such as mass transfer into dead-end pores, sorption, surfactant-enhanced solubilization and biodegradation.

Notation

A	column cross-sectional area (L^2)
a_{ec}	NAPL/water end-cap specific interfacial area (L^{-1})
A_{ec}	NAPL/water end-cap interfacial area (L^2)
A_{ec}^c	NAPL/water end-cap interfacial area in a chamber (L^2)
A_{ec}^t	NAPL/water end-cap interfacial area in a tube (L^2)
a_c	NAPL/water corner specific interfacial area (L^2)
A_c	NAPL/water corner interfacial area (L^2)
A_c^c	NAPL/water corner interfacial area in a chamber (L^2)
A_c^t	NAPL/water corner interfacial area in a tube (L^2)
a_i	NAPL/water total specific interfacial area (L^{-1})
A_i	interfacial area (L^2)
A_w	water cross-sectional area in network tube (L^2)
α_L	longitudinal dispersivity (L)
α_t	transverse dispersivity (L)
C	concentration ($M L^{-3}$)
C_{NAPL}	representation of NAPL phase as a solute concentration in BIOMOC ($M L^{-3}$)
C_s	solubility concentration ($M L^{-3}$)
d_{50}	median grain size (L)
d_M	diameter of a “medium” sand grain (L)
D	dispersion coefficient ($L^2 t^{-1}$)
D_m	molecular diffusion coefficient ($L^2 t^{-1}$)
F	solute flux ($M t^{-1}$)
J	dissolution flux ($M L^{-3} t^{-1}$)
K_1	half-saturation constant ($M L^{-3}$)
K_{cond}	hydraulic conductivity ($L t^{-1}$)
K_{diss}	dissolution coefficient ($L t^{-1}$)
K_{diss}^{ec}	end-cap dissolution coefficient ($L t^{-1}$)
K_{diss}^c	corner dissolution coefficient ($L t^{-1}$)
$K_{diss} a_i$	dissolution rate coefficient (t^{-1})
l_b	NAPL blob length (L)
l_c	chamber length (L)
l_t	tube length (L)
L	column length (L)
M	mass (M)
μ_w	water viscosity ($M L^{-1} t^{-1}$)
P_c	NAPL/water capillary pressure ($M L^{-1} t^{-2}$)
q_w	Darcy velocity ($L t^{-1}$)

Q_w	volumetric flow rate of the aqueous phase ($L^3 t^{-1}$)
Q'_w	aqueous phase flow per unit depth ($L^2 t^{-1}$)
r	pore radius (L)
r_c	chamber radius (L)
r_{Nw}	NAPL/water radius of curvature (L)
r_i	tube radius (L)
ρ_N	NAPL density ($M L^{-3}$)
ρ_w	water density ($M L^{-3}$)
σ_{Nw}	NAPL/water interfacial tension ($M t^{-2}$)
t	time (t)
v_w	average linear velocity ($L t^{-1}$)
v_{wc}	velocity in water corner ($L t^{-1}$)
V	porous media volume (L^3)
V_{max}	maximum uptake rate (t^{-1})
V_N	NAPL volume (L^3)
V_N^c	NAPL volume in a chamber (L^3)
V_N^t	NAPL volume in a tube (L^3)
x	distance (L)
ξ	corner length (L)

Dimensionless parameters

a_r	aspect ratio
α	multiple regression coefficient
β_1	multiple regression coefficient
β_2	multiple regression coefficient
β_3	multiple regression coefficient
β_4	multiple regression coefficient
δ	normalized grain size
ε	effective porosity
E_d	average corner concentration
ϕ	porosity
$Pe = (q_w d_{50})/D_m$	Peclet number
$Pe' = (v_w d_{50})/D_m$	modified Peclet number
$Re' = (v_w \rho_w d_{50})/\mu_w$	modified Reynolds number
S_N	NAPL saturation
S_{rN}	residual NAPL saturation
S_{rw}	residual water saturation
S_w	water saturation
t_d	dimensionless time
θ_{iN}	initial volumetric water content
θ_N	volumetric NAPL content
θ_w	volumetric water content
U_i	uniformity index

Acknowledgements

We would like to thank Susan Powers for making her dissolution data so readily accessible. We are grateful for Steve Gorelick's guidance and assistance on this project. We would also like to thank John Nimmo, Jon Johnson, and the reviewers, for their comments, which helped to significantly improve the manuscript. We gratefully acknowledge funding from the Western Region Hazardous Substances Research Program under contract SU95-3 (P.I.: S.M. Gorelick) of the Environmental Protection Agency. The content of this study does not necessarily represent the views of the agency. We are also grateful for funding provided by the Toxics Substances Hydrology Program of the US Geological Survey. Computer facilities were provided by a grant from the Hewlett-Packard Company and by NSF grant EAR-9707031 (P.I.s: S.M. Gorelick and K.Loague).

Appendix A. Representation and validation of NAPL dissolution in BIOMOC

The original BIOMOC code (Essaid et al., 1995; Essaid and Bekins, 1997) is a two-dimensional, multispecies solute-transport simulator of biodegradation. The steady-state flow equation is solved in each pumping period. The method of characteristics and particle tracking are used to solve the transport equation for each species. The Monod (1949) kinetics biodegradation reaction term implemented in BIOMOC has the following form:

$$\text{Consumption of solute } C = V_{\max} \left(\frac{C}{K1 + C} \right), \quad (\text{A.1})$$

where V_{\max} = the maximum uptake rate [t^{-1}]; $K1$ = the half-saturation constant [M L^{-3}]. Note that when $K1 \gg C$, consumption of solute C can be approximated by $(V_{\max}/K1)C$.

The code was easily adapted and modified to simulate NAPL dissolution. Immobile particle sets can be used to represent immobile phases. We assumed the NAPL phase was immobile and acted as a source of concentration of dissolved NAPL. Therefore, the NAPL phase was represented by an immobile particle set, and the dissolved NAPL was represented by a mobile particle set. The dissolution flux $J = K_{\text{diss}} a_i (C_s - C)$ was represented by the sum of two reactions. Reaction (1) represented consumption of the immobile NAPL phase. For reaction (1), the coefficient $(V_{\max}/K1)$ was set equal to $K_{\text{diss}} a_i$ multiplied by a coefficient $((1 - S_N)/(S_N \rho_N))$ that converted the concentration of the immobile NAPL phase to C_s . The concentration of the immobile NAPL phase, C_{NAPL} , was a function of NAPL saturation. Reaction (2) represented the consumption of the dissolved NAPL. For reaction (2), the coefficient $(V_{\max}/K1)$ was set equal to $K_{\text{diss}} a_i$. Thus, the net reaction represents the equation for NAPL dissolution flux:

$$J = K_{\text{diss}} a_i C_s \frac{1 - S_N}{S_N \rho_N} C_{\text{NAPL}} - K_{\text{diss}} a_i C, \quad (\text{A.2})$$

where reaction (1) = $K_{\text{diss}} a_1 C_s ((1 - S_N)/(S_N \rho_N)) C_{\text{NAPL}}$; reaction (2) = $K_{\text{diss}} a_1 C$; ρ_N = NAPL density [M L^{-3}]; $C_{\text{NAPL}} = ((S_N)/(1 - S_N)) \rho_N$ [M L^{-3}]; C = concentration of dissolved NAPL [M L^{-3}].

Another modification was that due to the presence of immobile NAPL phase, solute transport was a function of volumetric water content ($\theta_w = S_w \phi$) instead of porosity. Furthermore, θ_w increased as the immobile NAPL phase dissolved.

Calculation of NAPL dissolution using BIOMOC proceeded as follows. A particle step move was completed and new values of C and C_{NAPL} were calculated. New values of NAPL mass and S_N were computed based on this new value of C_{NAPL} and, a new value of θ_w was calculated using the new value of S_N . The mass balance equations for the immobile NAPL phase and dissolved NAPL were solved simultaneously.

We assumed that the water relative permeability was linear between 0.8 and 1.0 for water saturations between 0.9 and 1.0, respectively. Although the saturations and concentrations were updated every particle move, we designed BIOMOC to update the relative permeability every pumping period. A smaller pumping period resulted in increased accuracy due to more relative permeability updates, but more computation.

In previous investigations, BIOMOC was validated against analytic solutions to the one-dimensional transport equation with linear sorption, decay, and biodegradation, and against experimental and modeling results (Essaid et al., 1995; Essaid and Bekins, 1997). To ensure that the representation of dissolution in BIOMOC was realistic, we compared BIOMOC simulation results to the simulation results published by Powers et al. (1994b) for the dissolution of TCE in a model column having properties of a Wagner #18 sand. There was good agreement between the two simulation results. For both the Powers et al. (1994b) and BIOMOC simulations, the mass balance error was calculated as $100(1 - (\text{mass dissolved}/\text{mass leaving column}))$. For the Powers et al. (1994b) simulation, the mass balance error was reported to be less than 1% (Powers, 1992); for the BIOMOC simulation, the mass balance error was no greater than 3%.

References

- Anderson, M.R., Johnson, R.L., Pankow, J.F., 1992. Dissolution of dense chlorinated solvents into ground water: III. Modeling contaminant plumes from fingers and pools of solvent. *Environ. Sci. Technol.* 26 (5), 901–908.
- Borden, R.C., Kao, C.M., 1992. Evaluation of groundwater extraction for remediation of petroleum contaminated groundwater. *Water Environ. Res.* 64 (1), 28–36.
- Borden, R.C., Piwoni, M.D., 1992. Hydrocarbon dissolution and transport: a comparison of equilibrium and kinetic models. *J. Contam. Hydrol.* 10, 309–323.
- Bradford, S.A., Leij, F.J., 1997. Estimating interfacial areas for multi-fluid soil systems. *J. Contam. Hydrol.* 27 (1–2), 83–106.
- Brusseau, M.L., 1992. Rate-limited mass transfer and transport of organic solutes in porous media that contain immobile immiscible organic liquid. *Water Resour. Res.* 28 (1), 33–45.
- Carslaw, H.W., Jaeger, J.C., 1959. *Conduction of Heat in Solids*. 2nd edn. Clarendon Press, Oxford.
- Cary, J.W., 1994. Estimating the surface area of fluid phase interfaces in porous media. *J. Contam. Hydrol.* 15 (4), 243–248.
- Delshad, M., Pope, G.A., Sepehrnoori, K., 1996. A compositional simulator for modeling surfactant enhanced aquifer remediation: 1. Formulation. *J. Contam. Hydrol.* 23, 303–327.

- Deutsch, C.V., Journel, A.G., 1992. *GSLIB: Geostatistical Software Library and User's Guide*. Oxford Univ. Press, New York, NY.
- Dillard, L.A., Blunt, M.J., 2000. Development of a pore network model to study nonaqueous phase liquid dissolution. *Water Resour. Res.* 36 (2), 439–454.
- Dullien, F.A.L., 1992. *Porous Media: Fluid Transport and Pore Structure*. Academic Press, San Diego, CA.
- Essaid, H.I., Bekins, B.A., 1997. BIOMOC, a multispecies solute-transport model with biodegradation. *U.S. Geol. Surv. Water Resour.* 97–4022.
- Essaid, H.I., Bekins, B.A., Godsy, E.M., Warren, E., Baedeker, M.J., Cozzarelli, I.M., 1995. Simulation of aerobic and anaerobic biodegradation processes at a crude oil spill site. *Water Resour. Res.* 31 (12), 3309–3327.
- Geller, J.T., Hunt, J.R., 1993. Mass transfer from nonaqueous phase organic liquids in water-saturated porous media. *Water Resour. Res.* 29 (4), 833–845.
- Goode, D.J., Konikow, L.F., 1989. Modification of a method-of-characteristics solute-transport model to incorporate decay and equilibrium-controlled sorption or ion exchange. *U.S. Geol. Surv. Water Resour.* 89–4030.
- Guarnaccia, J.F., Imhoff, P.T., Missildine, B.C., Oostrom, M., Celia, M.A., Dane, J.H., Jaffe, P.R., Pinder, G.F., 1992. Multiphase chemical transport in porous media, Rep EPA/600/S-92/002, U.S. Environ. Protect. Agency, Kerr Environ. Res. Lab., Ada, OK.
- Gvirtzman, H., Roberts, P.V., 1991. Pore scale spatial analysis of two immiscible fluids in porous media. *Water Resour. Res.* 27 (6), 1165–1176.
- Hassanizadeh, S.M., Gray, W.G., 1990. Mechanics and thermodynamics of multiphase flow in porous media including interphase boundaries. *Adv. Water Resour.* 13, 169–186.
- Hassanizadeh, S.M., Gray, W.G., 1993. Thermodynamic basis of capillary pressure in porous media. *Water Resour. Res.* 29 (10), 3389–3405.
- Hess, K.M., Wolf, S.H., Celia, M.A., 1992. Large-scale natural gradient tracer test in sand and gravel, Cape Cod, Massachusetts: 3. Hydraulic conductivity variability and calculated macrodispersivities. *Water Resour. Res.* 28 (8), 2011–2027.
- Holman, H.-Y.N., Javandel, I., 1996. Evaluation of transient dissolution of slightly water-soluble compounds from a light nonaqueous phase liquid pool. *Water Resour. Res.* 32 (4), 915–923.
- Hunt, J.R., Sitar, N., Udell, K.S., 1988a. Nonaqueous phase liquid transport and cleanup: 1. Analysis of mechanisms. *Water Resour. Res.* 24 (8), 1247–1258.
- Hunt, J.R., Sitar, N., Udell, K.S., 1988b. Nonaqueous phase liquid transport and cleanup: 2. Experimental studies. *Water Resour. Res.* 24 (8), 1259–1269.
- Imhoff, P.T., Jaffe, P.R., Pinder, G.F., 1994. An experimental study of complete dissolution of a nonaqueous phase liquid in saturated porous media. *Water Resour. Res.* 30 (2), 307–320.
- Johnson, R.L., Pankow, J.F., 1992. Dissolution of dense chlorinated solvents into groundwater, 2. Source functions for pools of solvent. *Environ. Sci. Technol.* 26 (5), 896–901.
- Karkare, M.V., Fort, T., 1996. Determination of the air–water interfacial area in wet “unsaturated” porous media. *Langmuir* 12 (8), 2041–2044.
- Kennedy, C.A., Lennox, W.C., 1997. A pore-scale investigation of mass transport from dissolving DNAPL droplets. *J. Contam. Hydrol.* 24, 221–246.
- Kim, H., Rao, P.S., Annable, M.D., 1997. Determination of effective air–water interfacial area in partially saturated porous media using surfactant adsorption. *Water Resour. Res.* 33 (12), 2705–2711.
- Konikow, L.F., Bredehoeft, J.D., 1978. Computer model of two-dimensional solute transport and dispersion in ground water, *Techniques of Water Resources Investigations of the United States Geological Survey*. US Gov. Print. Off., Washington, DC, book 7, Chap. C2.
- Leverett, M.C., 1941. Capillary behavior in porous solids. *Trans. Am. Inst. Min., Metall. Pet. Eng.* 142, 152–169.
- Lowry, M.I., Miller, C.T., 1995. Pore-scale modeling of nonwetting-phase residual in porous media. *Water Resour. Res.* 31 (3), 455–473.
- Mackay, D., Shiu, W.Y., Majaneu, A., Feenstra, S., 1991. Dissolution of non-aqueous phase liquids in groundwater. *J. Contam. Hydrol.* 8, 23–42.
- Mayer, A.S., Miller, C.T., 1992. The influence of porous medium characteristics and measurement scale on pore-scale distributions of residual nonaqueous-phase liquids. *J. Contam. Hydrol.* 11, 189–213.

- Mayer, A.S., Miller, C.T., 1993. An experimental investigation of pore-scale distributions of nonaqueous phase liquids at residual saturation. *Transp. Porous Media* 10, 57–80.
- Mayer, A.S., Miller, C.T., 1996. The influence of mass transfer characteristics and porous media heterogeneity on nonaqueous phase dissolution. *Water Resour. Res.* 32 (6), 1551–1567.
- Miller, C.T., Poirier-McNeill, M.M., Mayer, A.S., 1990. Dissolution of trapped nonaqueous phase liquids: mass transfer characteristics. *Water Resour. Res.* 26 (11), 2783–2796.
- Monod, J., 1949. The growth of bacterial cultures. *Annu. Rev. Microbiol.* 3, 371–394.
- Montgomery, J.H., 1996. Second Edition Groundwater Chemicals Desk Reference. CRC Press, Boca Raton, FL.
- Parker, J.C., Katyal, A.K., Kaluarachchi, J.J., Lenhard, R.J., Johnson, T.J., Jayaraman, K., Unlu, K., Zhu, J.L., 1991. Modeling multiphase organic chemical transport in soils and ground water, Rep. EPA/600/2-91/042. US Environ. Protect. Agency, Washington, DC.
- Pfannkuch, H., 1984. Determination of the contaminant source strength from mass exchange processes at the petroleum–ground-water interface in shallow aquifer systems. *Proceedings NWWA/API Conf. of Petrol. Hydrocarbons and Organic Chemicals in Groundwater*, Houston. pp. 111–129.
- Powers, S.E., 1992. Dissolution of nonaqueous phase liquids in saturated subsurface systems. PhD Thesis, The University of Michigan. Ann Arbor, MI.
- Powers, S.E., Loureiro, C.O., Abriola, L.M., Weber, W.J., 1991. Theoretical study of the significance of nonequilibrium dissolution on nonaqueous phase liquids in subsurface systems. *Water Resour. Res.* 27 (4), 463–477.
- Powers, S.E., Abriola, L.M., Weber, W.J., 1992. An experimental investigation of nonaqueous phase liquid dissolution in saturated subsurface systems: steady state mass transfer rates. *Water Resour. Res.* 28 (10), 2691–2705.
- Powers, S.E., Abriola, L.M., Dunkin, J.S., Weber, W.J., 1994a. Phenomenological models for transient NAPL–water mass-transfer processes. *J. Contam. Hydrol.* 16, 1–33.
- Powers, S.E., Abriola, L.M., Weber, W.J., 1994b. An experimental investigation of NAPL dissolution in saturated subsurface systems: transient mass transfer rates. *Water Resour. Res.* 30 (2), 321–332.
- Priddle, M.W., MacQuarrie, K.T.B., 1994. Dissolution of creosote in groundwater: an experimental and model investigation. *J. Contam. Hydrol.* 15, 27–56.
- Reeves, P.C., Celia, M.A., 1996. A functional relationship between capillary pressure, saturation, and interfacial area as revealed by a pore-scale network model. *Water Resour. Res.* 32 (8), 2345–2358.
- Rosen, M.J., 1989. *Surfactants and Interfacial Phenomena*. 2nd edn. Wiley, New York.
- Saripalli, K.P., Annable, M.D., Rao, P.S.C., 1997a. Estimation of nonaqueous phase liquid–water interfacial areas in porous media following mobilization by chemical flooding. *Environ. Sci. Technol.* 31, 3384–3388.
- Saripalli, K.P., Kim, H., Suresh, P.S.C., Rao, C., Annable, M., 1997b. Measurement of specific fluid–fluid interfacial areas of immiscible fluids in porous media. *Environ. Sci. Technol.* 31 (3), 932–936.
- Saripalli, K.P., Rao, P.S.C., Annable, M.D., 1998. Determination of specific NAPL–water interfacial areas of residual NAPLs in porous media using the interfacial tracers technique. *J. Contam. Hydrol.* 30, 375–391.
- Schaefer, C.E., Blunt, M.J., 2000. Oil–water interfacial area of residual decane in saturated and unsaturated sand. *Water Resour. Res.* submitted for publication.
- Schaefer, C.E., DiCarlo, D.A., Blunt, M.J., 2000a. Determination of water–oil interfacial area during 3-phase gravity drainage in porous media. *J. Colloid Interface Sci.* 221, 308–312.
- Schaefer, C.E., DiCarlo, D.A., Blunt, M.J., 2000b. Experimental measurement of air–water interfacial area during gravity drainage and secondary imbibition in porous media. *Water Resour. Res.* in press.
- Seagren, E.A., Rittman, B.E., Valocchi, A.J., 1992. Quantitative evaluation of flushing and biodegradation for enhancing in situ dissolution of nonaqueous-phase liquids. *J. Contam. Hydrol.* 12, 103–132.
- Skopp, J., 1985. Oxygen uptake and transport in soils: analysis of the air–water interfacial area. *Soil Sci. Soc. Am. J.* 49 (6), 1327–1331.
- Sleep, B.E., Sykes, J.F., 1989. Modeling the transport of volatile organics in variably saturated media. *Water Resour. Res.* 25 (1), 81–92.
- VanderKwaak, J.E., Sudicky, E.A., 1996. Dissolution of non-aqueous-phase liquids and aqueous-phase contaminant transport in discretely fractured porous media. *J. Contam. Hydrol.* 23, 45–68.
- Voudrias, E.A., Assaf, K.S., 1996. Theoretical evaluation of dissolution and biochemical reduction of TNT for phytoremediation of contaminated sediments. *J. Contam. Hydrol.* 23, 245–261.

- Voudrias, E.A., Yeh, M., 1994. Dissolution of a toluene pool under constant and variable hydraulic gradients with implications for aquifer remediation. *Ground Water* 32 (2), 305–311.
- Whelan, M.P., Voudrias, E.A., Pearce, A., 1994. DNAPL pool dissolution in saturated porous media: procedure development and preliminary results. *J. Contam. Hydrol.* 15, 223–237.
- Zaidel, J., Russo, D., 1993. Analytical models of steady state organic species transport in the vadose zone with kinetically controlled volatilization and dissolution. *Water Resour. Res.* 29 (10), 3343–3356.
- Zhou, D., Dillard, L.A., Blunt, M.J., 2000. A physically based model of dissolution of nonaqueous phase liquids in the saturated zone. *Transp. Porous Media* 39 (2), 227–255.